

ITERATIVE AMORTIZED HIERARCHICAL VAE

S.W. Penninga[†], R.J.G. van Sloun

Eindhoven University of Technology, Department of Electrical Engineering
Eindhoven, The Netherlands
s.w.penninga@tue.nl[†]

ABSTRACT

In this paper we propose the Iterative Amortized Hierarchical Variational Autoencoder (IA-HVAE), which expands on amortized inference with a hybrid scheme containing an initial amortized guess and iterative refinement with decoder gradients. We achieve this by creating a linearly separable decoder in a transform domain (e.g. Fourier space), enabling real-time applications with very high model depths. The architectural change leads to a 35x speed-up for iterative inference with respect to the traditional HVAE. We show that our hybrid approach outperforms fully amortized and fully iterative equivalents in accuracy and speed respectively. Moreover, the IA-HVAE shows improved reconstruction quality over a vanilla HVAE in inverse problems such as deblurring and denoising.

Index Terms— Hierarchical VAE, Amortized inference, Iterative inference, Posterior inference, Inverse problems

1. INTRODUCTION

Inverse problems are a set of tasks in which the goal is to reconstruct a signal from degraded, incomplete, or noisy observations. Recently, interest has been sparked in addressing these tasks with deep generative models, since they can learn realistic high-dimensional priors and handle multi-modality.

A popular initial approach was to search for a plausible solution in the range of a Generative Adversarial Network (GAN) via gradient descent [1]. Later, this was surpassed by the current state-of-the-art Guided Diffusion [2] in terms of reconstruction quality. This method leverages pre-trained diffusion models and iteratively guides the diffusion process to the observations to achieve conditional sampling. While this has shown promising results in a wide range of domains [3, 4, 5], its application is bottle-necked by computational cost and the iterative backbone that cannot be parallelized.

We propose to instead use the Hierarchical Variational AutoEncoder (HVAE) [6] architecture for tasks where inference speed is crucial. This architecture has the potential to accelerate inference by initializing or replacing parts of the iterative process with a one-shot estimate for quicker convergence.

Although Variational AutoEncoders (VAEs) can perform rapid amortized inference, they have been largely overlooked for inverse problems as they are limited by an encoder that requires task-specific retraining which introduces an optimization bias. Next to this, they suffer from the *amortization gap*, the error between the amortized posterior and the optimal posterior estimate [7, 8]. While VAEs are theoretically capable of performing exact posterior inference, the necessity of a variational family refrains them from doing so [9, 10,

11]. This has sparked interest in hybrid schemes that combine amortization of the data distribution with iterative refinement for cheap and accurate inference, balancing speed and precision [12, 13]. The HVAE architecture should not be confused with these hybrid models. Instead of incorporating iterative inference, it's amortized inference process is unrolled into multiple conditional steps, which we will call *stacked inference*. Combining iterative optimization and stacked inference poses a challenge and requires architectural modifications to the HVAE as the computational cost of iterative optimization grows quadratically with the number of stochastic layers in the model. The performance of a HVAE relies heavily on having a large stochastic depth [14]. Just like the diffusion process, the stacked inference of the HVAE is autoregressive and cannot be parallelized, leading to increased computational cost and latency. However, the improved performance over the traditional VAE has led to current state-of-the-art models for density estimation [15, 16, 14, 17], outperforming even auto-regressive decoders [18] and diffusion models [19, 20], validating their potential for inference tasks and solving inverse problems.

In this paper we provide the first example of an Iterative Amortized HVAE (IA-HVAE), combining stacked inference of the HVAE with decoder gradient-based optimization. Inspired by latent aggregation [15], we propose to introduce a HVAE decoder with a linear separation in outputs, giving every latent layer access to the gradient of their contribution to the reconstruction without the need to evaluate the rest of the hierarchy. We will show that this leads to decreased computational cost and faster iterative optimization. The new architecture outperforms amortized inference in terms of accuracy, and fully iterative inference in terms of latency. Next to this, we provide examples of its use in inverse problems, such as deblurring and denoising.

2. METHODS

The goal of a VAE is to learn a joint distribution $p_{\theta}(x, z)$, usually factorized to $p_{\theta}(x|z)p_{\theta}(z)$ where x denotes a signal in the input domain and $z \in \mathbf{Z}$ a set of latent variables. They are trained with the Evidence Lower Bound (ELBO):

$$\log p_{\theta}(x) \geq \mathbb{E}_{q_{\phi}(z|x)} [\log p_{\theta}(x|z)] - D_{KL}[q_{\phi}(z|x)||p_{\theta}(z)], \quad (1)$$

in which θ denotes the set of generative model parameters and ϕ the set of inference model parameters. D_{KL} is the Kullback-Leibler divergence and for $p(z)$ we choose the Gaussian distribution.

2.1. Iterative Amortized Hierarchical VAE

We start with the HVAE architecture of the VDVAE [14] that follows the conditioning structure of the LadderVAE [6] in which the prior

This work was supported by the European Research Council (ERC) under the ERC starting grant nr. 101077368 (US-ACT).

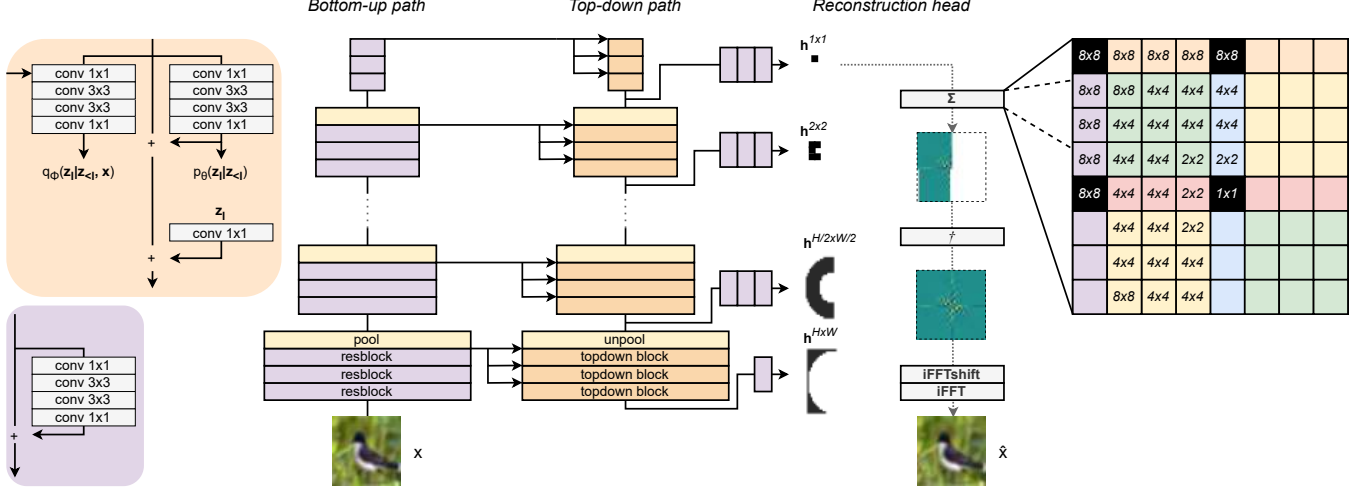


Fig. 1: Schematic overview of the IA-HVAE architecture. The layers in the orange and purple blocks are shown on the left. A mapping between the model scales and spatial frequency bins is shown on the right for an example with $H \times W = 8 \times 8$. Here the DC frequency is generated at the 1×1 scale and the Nyquist frequencies at 8×8 . The missing values are filled in with the hermitian conjugate[†] of the bins that share the same color to produce a symmetric spectrum and a purely real-valued image.

and approximate posterior are factorized in the same order:

$$p_\theta(\mathbf{z}) = p_{\theta_0}(\mathbf{z}_0)p_{\theta_1}(\mathbf{z}_1|\mathbf{z}_0)\dots p_{\theta_L}(\mathbf{z}_L|\mathbf{z}_{<L}), \quad (2)$$

$$q_\phi(\mathbf{z}|\mathbf{x}) = q_{\phi_0}(\mathbf{z}_0|\mathbf{x})q_{\phi_1}(\mathbf{z}_1|\mathbf{z}_0, \mathbf{x})\dots q_{\phi_L}(\mathbf{z}_L|\mathbf{z}_{<L}, \mathbf{x}). \quad (3)$$

Here, subscript l indexes the stochastic latent layer and its accompanying network modules, with $l \in [0, L]$. Because of the similarity between the HVAE and diffusion models [21], we emphasize that this entire paper can be understood through the lens of diffusion models. In this analogy, the weights of all θ_l are shared, $\mathbf{z}_l = \mathbf{x}_t$ and ϕ_l is replaced with a Gaussian noising process $\forall l$.

The reconstruction $p_\theta(\mathbf{x}|\mathbf{z})$ is traditionally done through a neural network, acting as a single non-linear function on all the latent vectors. Iterative posterior optimization through decoder gradients becomes intractable for deeper networks, since it requires the evaluation of all subsequent layers:

$$\nabla_{\mathbf{z}_l} p_\theta(\mathbf{x}|\mathbf{z}) = \nabla_{\mathbf{z}_L} p_\theta(\mathbf{x}|\mathbf{z}_L) + \sum_{l'=l}^L \nabla_{\mathbf{z}_{l'}} p_\theta(\mathbf{z}_{l'}|\mathbf{z}_{<l'}). \quad (4)$$

We propose to instead reconstruct \mathbf{x} as a linear combination \mathbf{B} of vectors \mathbf{h} in a discrete set \mathbf{H} through:

$$\mathbf{x}(\mathbf{z}) = \sum_{\mathbf{h} \in \mathbf{H}} \mathbf{B}\mathbf{h}(\mathbf{z}). \quad (5)$$

Now, the latent space is partitioned through a family of subsets $\{\mathbf{Z}_\mathbf{h}\}_{\mathbf{h} \in \mathbf{H}}$ with $\bigcup_{\mathbf{h} \in \mathbf{H}} \mathbf{Z}_\mathbf{h} = \mathbf{Z}$ and $\mathbf{Z}_\mathbf{h} \cap \mathbf{Z}_{\mathbf{h}'} = \emptyset$ ($\forall \mathbf{h} \neq \mathbf{h}'$) such that every \mathbf{h} is created from a separate $\mathbf{Z}_\mathbf{h}$, containing a unique $[\mathbf{z}_0, \dots, \mathbf{z}_M]$. Instead of using $\nabla_{\mathbf{z}_l} p_\theta(\mathbf{x}|\mathbf{z})$ we can now optimize a layer through:

$$\nabla_{\mathbf{z}_m} p_\theta(\mathbf{h}|\mathbf{z}) = \nabla_{\mathbf{z}_m} p_\theta(\mathbf{h}|\mathbf{z}_M) + \sum_{m'=m}^M \nabla_{\mathbf{z}_{m'}} p_\theta(\mathbf{z}_{m'}|\mathbf{z}_{<m'}). \quad (6)$$

2.2. Implementation details

The realization of \mathbf{H} is flexible and can be matched with the inference task. In this paper we focus on the task of 2D image generation. In this domain the latent variables \mathbf{z} do not necessarily share a

single spatial resolution and are usually distributed over several network scales s in order to capture both global and local structures. For example, the first latent vector \mathbf{z}_0^s is often of scale 1×1 and represents the DC frequency. The final latent \mathbf{z}_L matches the data resolution $H \times W$ and is able to represent anything from DC to high-frequency noise [22]. This implicitly creates an ordering where the lowest frequency is created first, and higher order frequencies are conditionally generated through $p_\theta(\mathbf{z}^s|\mathbf{z}^{s-1})$. In this example implementation we copy this ordering for the decomposition, use the FFT as \mathbf{B} , and generate images in the frequency domain such that $\mathbf{H} = \{\mathbf{h}^{1 \times 1}, \mathbf{h}^{2 \times 2}, \dots, \mathbf{h}^{H \times W}\}$ where every \mathbf{h} contains the spatial frequencies of the respective scale. For domains that operate with real-valued signals, we predict only the half-spectrum, and obtain the full spectrum using the hermitian conjugate (\dagger). A schematic overview of the architecture for real-valued signals together with an example of this frequency mapping $\mathbf{H} \rightarrow \hat{\mathbf{x}}$ is shown in Fig. 1.

2.3. Iterative optimization

Performing iterative optimization of \mathbf{z} solely with decoder gradients can move the latent vector off manifold and create instabilities for subsequent layers in the conditioning chain. We sample the distribution and refine the latent vector with Maximum A Posteriori (MAP) estimation. Using the negative log-likelihood (NLL) of the sample with respect to the prior we obtain the following update rule for a single latent vector:

$$\mathbf{z}_l^{n+1} = \mathbf{z}_l^n - \lambda \nabla_{\mathbf{z}_l^n} \left[\log \mathcal{N}(\mathbf{z}_l^n; \mu_p, \sigma_p) + \beta \mathcal{L}(\mathbf{h}^{s_l}, \hat{\mathbf{h}}^{s_l}) \right]. \quad (7)$$

Here λ is the step size of the update, μ_p and σ_p parameterize the prior distribution, \mathcal{L} denotes a loss function and β is a weight resembling guidance strength of the reconstruction. During the inference process, we sequentially update all latent vectors of the hierarchy in a Top-Down ordering. The complete inference process including an amortized pass is shown in Algorithm 1.

Algorithm 1 Inference sequence for the Iterative Amortized HVAE

Require: input \mathbf{x} , encoder parameters $\phi = [\phi_0, \dots, \phi_L]$, decoder parameters $\theta = [\theta_0, \dots, \theta_L]$, linear transformation \mathbf{B} , number of iterations N , subset length M , guidance strength β , step size λ , reconstruction loss function \mathcal{L} .

```

 $[\mathbf{h}^{1 \times 1}, \dots, \mathbf{h}^{H \times W}] \leftarrow \mathbf{B}^{-1} \mathbf{x}$   $\triangleright$  Linear decomposition targets
 $\hat{\mathbf{h}}_0 \leftarrow \mathbf{0}$   $\triangleright$  Initialize zero context vector
for  $l = 1 : L$  do
     $\mathbf{z}_l^1 \leftarrow q_{\phi_l}(\hat{\mathbf{h}}_{l-1}, \mathbf{x})$   $\triangleright$  Single amortized pass
     $\mu_p, \sigma_p \leftarrow p_{\theta_l}(\hat{\mathbf{h}}_{l-1})$   $\triangleright$  Prior  $p_{\theta}(\mu_p, \sigma_p | \hat{\mathbf{h}}_{l-1})$  for every  $l$ 
    for  $n = 1 : N$  do
         $\hat{\mathbf{h}}_l \leftarrow p_{\theta_l}(\hat{\mathbf{h}}_{l-1}, \mathbf{z}_l^n)$   $\triangleright$  Add contribution of latent  $\mathbf{z}_l^n$ 
        for  $m = 1 : M$  do  $\triangleright$  Complete scale with subset  $Z_h$  (6)
             $\hat{\mathbf{h}}_l \leftarrow p_{\theta_m}(\hat{\mathbf{h}}_l, \mathbf{z}_m)$ 
        end for
         $\mathbf{z}_l^{n+1} \leftarrow \mathbf{z}_l^n - \lambda \nabla_{\mathbf{z}_l^n} [\log \mathcal{N}(\mathbf{z}_l^n; \mu_p, \sigma_p) + \beta \mathcal{L}(\mathbf{h}^{s_l}, \hat{\mathbf{h}}_l)]$ 
    end for
     $\hat{\mathbf{x}} \leftarrow \sum_h \mathbf{B} \mathbf{h}$ 
return  $\hat{\mathbf{x}}, \mathbf{z}$ 

```

Note: superscript denotes iterative step number n for \mathbf{z} , and the scale of the current layer s_l for \mathbf{h} .

3. EXPERIMENTS & RESULTS

First, in Section 3.2 we compare the iterative inference time of the IA-HVAE (6) with the vanilla HVAE architecture (4). Then in Section 3.3 we compare the inference quality of the vanilla amortized HVAE with that of a fully iterative inference using the IA-HVAE and the hybrid inference of the IA-HVAE. Lastly, the HVAE and the hybrid IA-HVAE are compared on inverse problems in Section 3.4. To test performance on both real-valued and complex signals, we use CIFAR10 [23] (32×32 pixels) and fastMRI [24] (rescaled to 128×128 pixels) respectively.

3.1. Experimental setup

For both datasets we train a model on the standardized train split and report the results on the test split. For CIFAR10 and fastMRI we have 6 and 8 scales respectively to populate all spatial frequencies. For CIFAR10 the model produces 3 half-spectra (real and imaginary values for every RGB channel) and for fastMRI a whole spectrum, as described in Section 2.2. Across all experiments the residual blocks have 128 outer and 64 inner channels with the swish activation function. The Bottom-up path and Reconstruction head of Fig. 1 have 3 residual blocks per scale. For every latent vector we choose a channel size of 1 to maximize Active Units [25] in the model. We empirically find that a high number of Active Units corresponds to more efficient iterative optimization, because the vectors reside in a more compressed domain. All models are trained with a pixel-wise MSE loss and subsequent iterative refinement is done with an L1 loss on \mathbf{H} with $\lambda = 0.001$ and $\beta = 1$ for all layers. All results are gathered on a single NVIDIA GeForce 2080 Ti GPU, coded in Keras 3.10.0 [26] with the Tensorflow 2.19.0 [27] backend and XLA compiler. The comparisons between inference methods are done on the same model with the same weights.

3.2. Inference time

A comparison of the inference time between the vanilla HVAE and the IA-HVAE is shown in Fig. 2.

For both datasets we show the execution time of a single amortized pass and that of 25 iterative refinement steps. The fact that there is no difference in timing between the datasets confirms that inference speed is limited solely by the model depth.

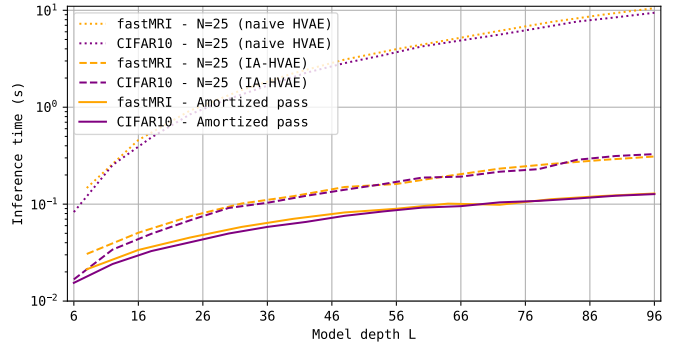


Fig. 2: Inference time comparison between the vanilla HVAE architecture and the IA-HVAE architecture for different model depths.

The IA-HVAE shows favourable scaling with respect to depth, leading to a 35x speedup for deeper networks. This performance gain would be even greater if the computational resources were saturated, as the vanilla HVAE architecture requires the entire model to be present in memory every iteration, leading to additional overhead.

3.3. Inference quality

To test inference quality we train a model for both datasets with 5 stochastic layers per scale ($L=30$ & $L=40$). A visualization of the IA-HVAE output is shown in Fig. 3 at every scale, showing the frequency-wise conditioning in the generation process.

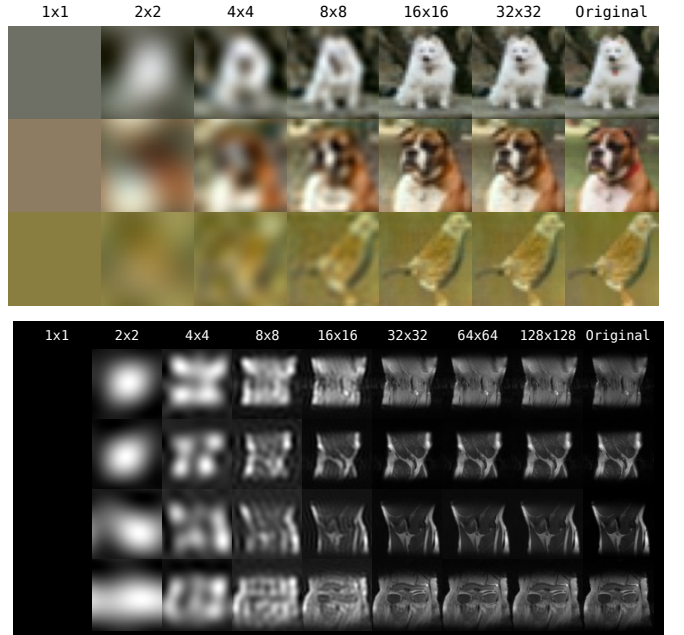


Fig. 3: Visualization of the IA-HVAE ($N=25$) output at multiple scales for CIFAR10 and fastMRI. Best viewed zoomed in.

Table 1: Quantitative comparison of inference methods: amortized inference is the HVAE, iterative and hybrid inference the IA-HVAE.

Method	N	CIFAR10 ($L=30$)				fastMRI ($L=40$)			
		MSE \downarrow	NLL (nats/dim) \downarrow	FID \downarrow	Time (s) \downarrow	MSE \downarrow	NLL (nats/dim) \downarrow	FID \downarrow	Time (s) \downarrow
<i>Amortized inference</i>	0	18.27	0.86	31.6	0.051	161.2	0.69	47.1	0.081
<i>Iterative inference</i>	5	29.10*	0.43*	77.6*	<u>0.068</u>	228.5*	0.44*	98.2*	<u>0.093</u>
	10	24.91*	<u>0.65*</u>	55.4*	0.074	192.4*	<u>0.48*</u>	87.3*	0.102
	20	22.75	0.71	37.0	0.095	155.6	0.60	46.5	0.131
	25	20.54	0.73	34.5	0.103	152.1	0.61	46.2	0.142
	50	18.01	0.78	31.0	0.193	150.5	0.61	46.2	0.266
<i>Hybrid inference</i>	5	18.09	0.84	31.2	0.130	158.2	0.65	47.0	0.162
	10	18.02	0.83	31.0	0.134	153.3	0.62	46.4	0.169
	20	17.91	0.82	30.9	0.149	149.6	0.61	46.1	0.186
	25	<u>17.86</u>	0.80	<u>30.8</u>	0.156	<u>148.2</u>	0.60	<u>45.9</u>	0.192
	50	17.84	0.80	30.8	0.241	145.0	0.59	45.5	0.293

Best performance shown in **bold**; second-best shown underlined. Note that VAEs optimize for likelihood in training and not perceptual sharpness.

* A high MSE or FID with low NLL shows that iterative inference has not yet converged and the model is sampling close to the prior.

A quantitative comparison is shown in Table 1. Note that the fastMRI dataset distribution is far more structured and less complex than CIFAR10. For this reason, iterative inference requires fewer iterations to converge. Nevertheless, for both datasets the hybrid approach always outperforms the amortized method in inference quality and can equate the quality of iterative inference in less time.

3.4. Inverse problems

In this section we qualitatively compare the IA-HVAE ($N=25$) performance to the vanilla HVAE on two inverse problems for the fastMRI dataset. First we test deblurring. We measure a subset of the spatial frequency bins in an image up to 8×8 and set others to 0. Since in MRI k-space coefficients are measured directly, this can also be interpreted as a compressed sensing setup. With both models we perform inference up until the 8×8 scale, after which we continue reconstruction with the prior. Next, we test a *denoising* problem, in which we add $\mathcal{N}(0, 1)$ noise to the model input which is normalized to the zero mean and unit variance. The reconstruction results for both experiments are shown in Fig. 4 together with log-magnitude k-space representations.

The IA-HVAE outperforms the vanilla HVAE in both experiments. With better inference it provides a better reconstruction for the deblurring example. It is also more successful in handling noisy images, since it is able to move latent vectors back to the data manifold when an amortized posterior estimate fails.

4. DISCUSSION AND CONCLUSION

Our implementation of the IA-HVAE with a frequency separated \mathbf{H} outperformed the vanilla HVAE in inference quality and has shown promising application in deblurring and denoising. Future work could investigate layer or scale specific finetuning of N to further decrease inference time. We expect tasks that benefit from hierarchical conditioning, such as sequential and separable acquisition tasks, to benefit greatly from a specialized IA-HVAE implementation.

One such example is any measurement over time that involves low frequency motion. The current diffusion-based methods require many noising steps to accommodate this type of pixel-wise translation in between frames, whereas the IA-HVAE can permute the latent layers at lower scales to express this phenomenon directly.

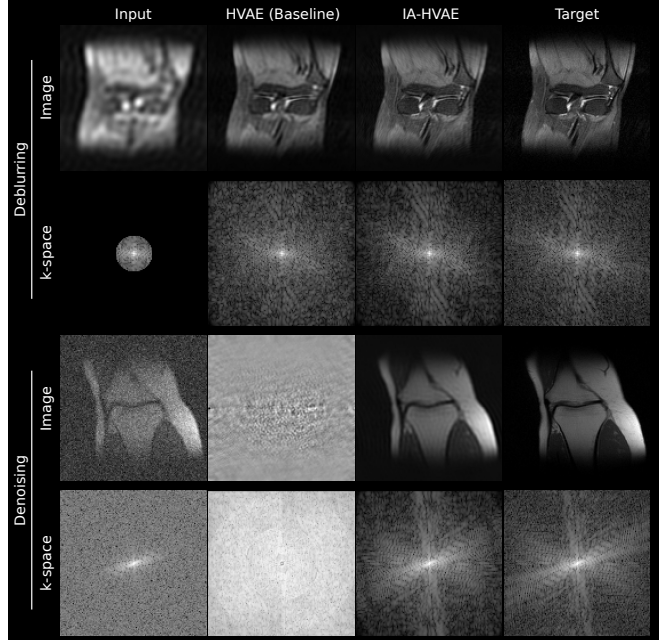


Fig. 4: Qualitative evaluation of the IA-HVAE ($N=25$) and vanilla HVAE (baseline) for deblurring and denoising experiments.

An obvious downside to the proposed approach is that the signal needs to be linearly decomposable. While this is possible for most fully sampled signals by moving to the frequency domain, this representation of the data can be more complex and harder for the model to learn. For future work, we suggest to research a more generalizable linear decomposition of signals that is still aligned with the Top-Down hierarchical nature of the model.

Other future work includes the incorporation of iterative optimization into the training process. Performing decoder-based refinement before the backward pass and weight update of the encoder will likely tighten the ELBO of the model. We leave a quantitative comparison with other generative architectures for future research.

5. REFERENCES

- [1] Ashish Bora, Ajil Jalal, Eric Price, and Alexandros G Dimakis, “Compressed Sensing using Generative Models,” in *Proceedings of the 34th International Conference on Machine Learning*, Doina Precup and Yee Whye Teh, Eds. 9 2017, vol. 70 of *Proceedings of Machine Learning Research*, pp. 537–546, PMLR.
- [2] Hyungjin Chung, Jeongsol Kim, and Jong Chul Ye, “Diffusion models for inverse problems,” *arXiv preprint arXiv:2508.01975*, 2025.
- [3] Tristan Stevens, Hans van Gorp, Faik C Meral, Junseob Shin, Jason Yu, Jean-luc Robert, and Ruud Van Sloun, “Removing Structured Noise using Diffusion Models,” *Transactions on Machine Learning Research*, 2025.
- [4] Giannis Daras, Weili Nie, Karsten Kreis, Alexandros G Dimakis, Morteza Mardani, Nikola B Kovachki, and Arash Vahdat, “Warped Diffusion: Solving Video Inverse Problems with Image Diffusion Models,” in *Advances in Neural Information Processing Systems*, A Globerson, L Mackey, D Belgrave, A Fan, U Paquet, J Tomczak, and C Zhang, Eds. 2024, vol. 37, pp. 101116–101143, Curran Associates, Inc.
- [5] Morteza Mardani, Jiaming Song, Jan Kautz, and Arash Vahdat, “A variational perspective on solving inverse problems with diffusion models,” *arXiv preprint arXiv:2305.04391*, 2023.
- [6] Casper Kaae Sønderby, Tapani Raiko, Lars Maaløe, Søren Kaae Sønderby, and Ole Winther, “Ladder variational autoencoders,” in *Advances in Neural Information Processing Systems*, 2016, vol. 0.
- [7] Rahul Krishnan, Dawen Liang, and Matthew Hoffman, “On the challenges of learning with inference networks on sparse, high-dimensional data,” in *Proceedings of the Twenty-First International Conference on Artificial Intelligence and Statistics*, Amos Storkey and Fernando Perez-Cruz, Eds. 7 2018, vol. 84 of *Proceedings of Machine Learning Research*, pp. 143–151, PMLR.
- [8] Chris Cremer, Xuechen Li, and David Duvenaud, “Inference Suboptimality in Variational Autoencoders,” in *Proceedings of the 35th International Conference on Machine Learning*, Jennifer Dy and Andreas Krause, Eds. 7 2018, vol. 80 of *Proceedings of Machine Learning Research*, pp. 1078–1086, PMLR.
- [9] Matthew D Hoffman and Matthew J Johnson, “Elbo surgery: yet another way to carve up the variational evidence lower bound,” in *Workshop in Advances in Approximate Bayesian Inference*. 2016, NIPS.
- [10] Mihaela Rosca, Balaji Lakshminarayanan, and Shakir Mohamed, “Distribution matching in variational inference,” *arXiv preprint arXiv:1802.06847*, 2018.
- [11] Yixin Wang, David M. Blei, and John P. Cunningham, “Posterior Collapse and Latent Variable Non-identifiability,” in *Advances in Neural Information Processing Systems*, 2021, vol. 7.
- [12] Joseph Marino, Yisong Yue, and Stephan Mandt, “Iterative amortized inference,” in *35th International Conference on Machine Learning, ICML 2018*, 2018, vol. 8.
- [13] Hadi Vafaii, Dekel Galor, and Jacob L Yates, “Brain-like variational inference,” *ArXiv*, p. arXiv-2410, 2025.
- [14] Rewon Child, “Very Deep VAEs Generalize Autoregressive Models and Can Outperform Them on Images,” in *ICLR 2021 - 9th International Conference on Learning Representations*, 2021.
- [15] Anna Kuzina and Jakub M Tomczak, “Hierarchical VAE with a Diffusion-based VampPrior,” *Transactions on Machine Learning Research*, vol. 2024, pp. 1–21, 2024.
- [16] Ifigeneia Apostolopoulou, Ian Char, Elan Rosenfeld, and Artur Dubrawski, “Deep Attentive Variational Inference,” in *ICLR 2022 - 10th International Conference on Learning Representations*, 2022.
- [17] Arash Vahdat and Jan Kautz, “NVAE: A deep hierarchical variational autoencoder,” in *Advances in Neural Information Processing Systems*, 2020, vol. 2020-December.
- [18] Rewon Child, Scott Gray, Alec Radford, and Ilya Sutskever, “Generating long sequences with sparse transformers,” *arXiv preprint arXiv:1904.10509*, 2019.
- [19] Jonathan Ho, Ajay Jain, and Pieter Abbeel, “Denoising diffusion probabilistic models,” *Advances in neural information processing systems*, vol. 33, pp. 6840–6851, 2020.
- [20] Diederik Kingma, Tim Salimans, Ben Poole, and Jonathan Ho, “Variational diffusion models,” *Advances in neural information processing systems*, vol. 34, pp. 21696–21707, 2021.
- [21] Calvin Luo, “Understanding diffusion models: A unified perspective,” *arXiv preprint arXiv:2208.11970*, 2022.
- [22] Louay Hazami, Rayhane Mama, and Ragavan Thurairatnam, “Efficientvdvae: Less is more,” *arXiv preprint arXiv:2203.13751*, 2022.
- [23] Alex Krizhevsky, “Learning Multiple Layers of Features from Tiny Images,” ... *Science Department, University of Toronto, Tech.* ..., 2009.
- [24] Jure Zbontar, Florian Knoll, Anuroop Sriram, Tullie Murrell, Zhengnan Huang, and Matthew J Muckley et al., “fastMRI: An Open Dataset and Benchmarks for Accelerated MRI,” *CoRR*, vol. abs/1811.08839, 2018.
- [25] Yuri Burda, Roger Grosse, and Ruslan Salakhutdinov, “Importance weighted autoencoders,” in *4th International Conference on Learning Representations, ICLR 2016 - Conference Track Proceedings*, 2016.
- [26] François Chollet and others, “Keras,” <https://keras.io>, 2015.
- [27] Martin Abadi, Ashish Agarwal, Paul Barham, Eugene Brevdo, Zhifeng Chen, and Craig Citro et al., “TensorFlow: A system for large-scale machine learning,” in *Proceedings of the 12th USENIX Symposium on Operating Systems Design and Implementation, OSDI 2016*, 2016.